Materials Research Proceedings 41 (2024) 467-476 https://doi.org/10.21741/9781644903131-52

Strain gradient calculation as a basis for localized roving slip prediction in macroscopic forming simulation of non-crimp fabrics

WANK Jan Paul[1,a *], SCHÄFER Bastian[1], MITSCH Johannes[1] and KÄRGER Luise[1]

[1]Karlsruhe Institute of Technology (KIT), Institute of Vehicle System Technology (FAST) – Lightweight Engineering, 76131 Karlsruhe, Germany

[a]jan.wank@kit.edu

Keywords: Non-Crimp Fabrics, Forming Simulation, Local Effects

Abstract. The utilization of the Finite Element Method (FEM) in forming simulation presents the possibility for a thorough examination of the deformation behavior exhibited by engineering textiles during the draping processes. In macroscopic forming simulations the relevant forming effects are depicted in a homogenized way. Slippage of fibers is an essential deformation mechanism of non-crimp fabrics (NCF). Experimentally, this is already observed at coupon level performing the bias-extension test (BET). Significant slippage occurs locally in the transition areas between shear zones with deviating shear angles. In existing macroscopic simulation approaches, roving slippage is only considered homogenized over the shear zones. A localized slip between individual fiber rovings cannot be modelled. Therefore, in the present work a neighboring element method for ABAQUS/EXPLICIT is introduced. This method uses multiple subroutines to transfer information between elements. The functionality of the neighboring method is confirmed by calculating a cross element gradient of the shear angle. The calculation of the shear angle gradient is shown in the simulation of the BET, giving rise to the transition zones which have been experimentally highlighted.

Introduction

Lightweight construction is a holistic development concept that aims to reduce the mass of a system while taking economic and ecological constraints into account [1]. Due to their fiber architecture continuous fiber-reinforced composites offer great potential for lightweight construction. A deep understanding of the draping process of engineering textiles is necessary to achieve optimal component design. The FEM is a proven method for simulating the forming behavior and process-induced defects of fiber-reinforced composites.

Due to their difference in fiber architecture, woven fabrics and NCF exhibit different draping behavior. While woven fabrics have an intrinsic cohesion, for NCF this is realized extrinsically through the stitching, resulting in straight fibers without undulations. Therefore, the shear behavior and thus the forming behavior of NCF is strongly dependent on the position of the stitching. Compared to bidirectional NCF the forming of unidirectional (UD-) NCF is predominantly influenced by simple shear rather than pure shear [2], leading to a more challenging draping process. The very high longitudinal stiffness of UD-NCF brings a greater degree of susceptibility for localized draping effects such as fiber gapping, slippage of fiber rovings and waviness or fiber curvature [3–6].

To determine the forming behavior of fiber-reinforced composites, commonly experimental tests are carried out. The BET is widely used to characterize the in-plane shear behavior of fabrics. For the BET, the pin-jointed net assumption is often made, which assumes that fiber crossings act as rotational knots and that fibers are inextensible [7]. This assumption is generally recognized for woven fabrics and results in a deformation with three distinct shear zones [4,7,8]. For woven fabrics, in one of the zones pure shear occurs. In the second zones only half of the shear from the

first zone occurs, while in the third zones no shear deformation arises. Although NCF do not have fiber crossings and therefore the kinematic assumption of pure rotation is not valid, the BET is still used for characterizing the in-plane shear behavior. While applying the BET on bidirectional NCF it can be observed that roving slippage occurs in the transition of the shear zones defining areas with a deviation of the shear angle [9]. It has been shown experimentally that when performing the BET on UD-NCF the different zones are less distinct from each other and more zones between high shear and zero shear occur [6,10].

To simulate technically relevant parts in forming accurately, simulation models at a macroscopic level of detail are necessary. Due to better drapability, the focus in macroscopic simulation models has historically been set on woven fabrics [11–15]. Simulations of NCF have mostly been carried out on the mesoscopic level [3,16–18]. In mesoscopic simulations, the fibers and the stitching are modeled discretely and thus locally occurring forming effects can be explicitly resolved. More recently, simulation models for NCF have been developed also on a macroscopic scale [19–22]. In order to depict the relevant forming mechanisms occurring on the meso-scale, macroscopic approaches need to capture them in a homogenized way. This results in predictions of areas with a high likelihood of the occurrence of local effects. These approaches locally assume constant material properties for each element. Therefore, effects induced by their surroundings like strain gradients are not considered.

The consideration of localized forming effects in macroscopic simulations induces the need for a neighboring element method. This paper will present the implemented framework of such a method within the commercial FEM solver ABAQUS/EXPLICIT by using multiple user subroutines and allocatable arrays. It has been experimentally documented that roving slippage occurs while conducting the BET for NCF [9]. To the best of the authors' knowledge, there is no macroscopic model that considers localized roving slippage for NCF. Since the area of occurrence is limited to areas with a large gradient of the shear angle, a method is developed to determine a spatial gradient from a scalar quantity inside a FORTRAN subroutine. The cross element gradient calculation is used to demonstrate the functionality of the framework for the neighboring method and is applied to simulation of the BET.

Gradient calculation based on a neighboring element method

To consider the modelling of localized draping effects in macroscopic forming simulations, non-local information in the onset area of the effects needs to be known. For woven fabrics such a non-local method has already been utilized by Steer et al. [23]. They calculate the in-plane curvature of the fibers by passing a fictive Bernoulli beam through a reference element and its neighbor element by using a neighboring element method.

ABAQUS/EXPLICIT has been utilized as a simulation tool for draping simulation of various fabrics [6,12,13,20,24]. Since there is no built-in method for determining the neighboring relationships between elements, the implemented method will be presented in the following [25]. Additionally, it will also be shown how a cross element spatial gradient is calculated from a scalar quantity based on the non-local framework.

*Neighboring element method***.** The implemented non-local framework combines user subroutines and regular FORTRAN subroutines. Since external subroutines are used, the user subroutine VEXTERNALDB is needed. This subroutine is called multiple times during the analysis and enables the call of external programs as well as the data transfer between external and user subroutines. While submitting an analysis within ABAQUS the so-called input file is written out. This file establishes the foundation of the neighboring method, as it contains the discretization and thereby the element-node relationship. The input file is read in and processed in external subroutines. After processing the mesh information, the element-to-element connection is determined and stored in global arrays to make them accessible within other subroutines.

Gradient calculation. The construction of a cross element spatial gradient from an element-based scalar field variable is commonly applied for solving computational fluid dynamic problems. An extensively investigated and commonly used method is the cell-average weighted least-squares (WLSQ) gradient method [26,27]. The WLSQ gradient method will be derived below and the adaptions for the draping simulation will be shown. The derivation is performed for an arbitrary number of neighbor elements while the implementation will only consider the stencil of first edge neighbors (en1) as shown in Figure 1.

Starting point for the WLSQ gradient method yields the first-order Taylor series expansion of the shear angle γ

$$\gamma_J = \gamma_I + \nabla\gamma_I \cdot \boldsymbol{d}_{IJ} + H \tag{1}$$

with γ_I and γ_J being the shear angle on the respective element I, J and $\nabla\gamma_I$ being the spatial gradient of the element I in x-, y- and z-direction. The higher-order terms of the Taylor series H are neglected in the following. The variable $\boldsymbol{d}_{IJ}$ is the direction vector from centroid of element I to centroid of element J.

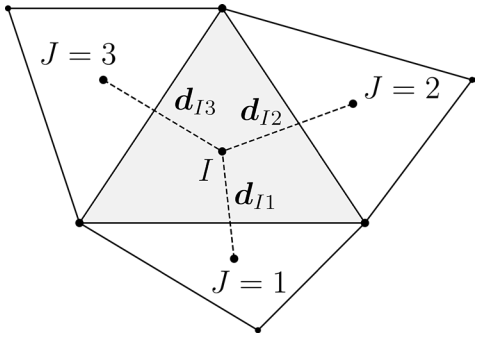

Fig. 1: Stencil of first edge neighbors (en1) showing the reference element I (grey) and its neighboring elements J.

It is worth noting that the indexes in capital letters are not indexes in the context of Einstein's summation convention but serve to identify the reference element I and the neighboring elements J. For an arbitrary number of elements N this leads to an overdetermined linear system of the form

$$\begin{bmatrix} \boldsymbol{d}_{I1}^{\top} \\ \boldsymbol{d}_{I2}^{\top} \\ \vdots \\ \boldsymbol{d}_{IN}^{\top} \end{bmatrix} \begin{bmatrix} \partial\gamma/\partial x \\ \partial\gamma/\partial y \\ \partial\gamma/\partial z \end{bmatrix}_I = \begin{bmatrix} \Delta x_{I1} & \Delta y_{I1} & \Delta z_{I1} \\ \Delta x_{I2} & \Delta y_{I2} & \Delta z_{I2} \\ \vdots & \vdots & \vdots \\ \Delta x_{IN} & \Delta y_{IN} & \Delta z_{IN} \end{bmatrix} \begin{bmatrix} \partial\gamma/\partial x \\ \partial\gamma/\partial y \\ \partial\gamma/\partial z \end{bmatrix}_I = \begin{bmatrix} \Delta\gamma_{I1} \\ \Delta\gamma_{I2} \\ \vdots \\ \Delta\gamma_{IN} \end{bmatrix} \tag{2}$$

which can be summarized as $\boldsymbol{D}\nabla\gamma_I = \boldsymbol{b}$. The operator Δ can be interpreted as $\Delta(\cdot)_{IJ} = (\cdot)_J - (\cdot)_I$. As large element aspect ratios can be attained during the draping simulation, stabilization in the form of weights is introduced to Eq. (2), resulting in

$$\boldsymbol{W}\boldsymbol{D}\nabla\gamma_I = \boldsymbol{W}\boldsymbol{b}. \tag{3}$$

The weighting matrix $\boldsymbol{W}$ is a diagonal matrix containing the weights $w_{iiJ} = 1/\|\boldsymbol{d}_{IJ}\|^{\mathrm{p}}$ with $i = 1, \dots, N$ and the parameter p. Solving the system of Eq. (3) is done by multiplying both sides from the left with $\boldsymbol{D}^{\top}\boldsymbol{W}$. This results in the left-hand side having a quadratic form and therefore it can be inversed. This leads to

Materials Research Proceedings 41 (2024) 467-476 https://doi.org/10.21741/9781644903131-52

$$\nabla\gamma_I = (\boldsymbol{D}^\top \boldsymbol{W}\boldsymbol{W}\boldsymbol{D})^{-1}\boldsymbol{D}^\top \boldsymbol{W}\boldsymbol{W}\boldsymbol{b}. \tag{4}$$

From Eq. (4) it can be seen that through the matrix $\boldsymbol{D}$ and its transpose the distance between the centroids is squared in the first inverted part while it is only linear in the second part. This yields a dependency of the dimension of the gradient on the element size of the mesh. To circumvent this, the matrix $\boldsymbol{D}$ is normed as follows

$$\boldsymbol{D}_{\text{norm}} = \begin{bmatrix} \boldsymbol{d}_{I1}^\top / \|\boldsymbol{d}_{I1}\| \\ \boldsymbol{d}_{I2}^\top / \|\boldsymbol{d}_{I2}\| \\ \vdots \\ \boldsymbol{d}_{IN}^\top / \|\boldsymbol{d}_{IN}\| \end{bmatrix} = \begin{bmatrix} \boldsymbol{d}_{\text{norm},I1}^\top \\ \boldsymbol{d}_{\text{norm},I2}^\top \\ \vdots \\ \boldsymbol{d}_{\text{norm},IN}^\top \end{bmatrix}. \tag{5}$$

The vector $\boldsymbol{d}_{\text{norm},IJ}$ and the matrix $\boldsymbol{D}_{\text{norm}}$ therefore only contain directional information. The matrix $\boldsymbol{D}_{\text{norm}}$ is substituted into Eq. (4) instead of $\boldsymbol{D}$.

Calculating the gradient using the WLSQ method leads to the gradient components expressed in the global configuration $\{\boldsymbol{e}_i\}$. To utilize the gradient in the context of forming simulation its components need to be expressed in the current configuration $\{\boldsymbol{a}_i\}$. Figure 2 exemeplifies the transformation between the different configurations, resulting in the non-orthogonal principal material orientations $\{\boldsymbol{a}_i\}$ in the current configuration. Since the initial fiber orientation $\{\boldsymbol{A}_i\}$ does not have to be aligned with the global configuration, a preceding transformation is necessary. Based on the assumption of a cross-ply NCF this transformation is a simple orthogonal rotation $\boldsymbol{R}$. The deformation gradient $\boldsymbol{F}$ relates the initial $\{\boldsymbol{A}_i\}$ and the current configuration $\{\boldsymbol{a}_i\}$. Therefore, the gradient components with respect to the current configuration are obtained through

$$\nabla\gamma_{i,\{\boldsymbol{a}_i\}} = (FR)_{ij}^{-1}\nabla\gamma_{j,\{\boldsymbol{e}_i\}}. \tag{6}$$

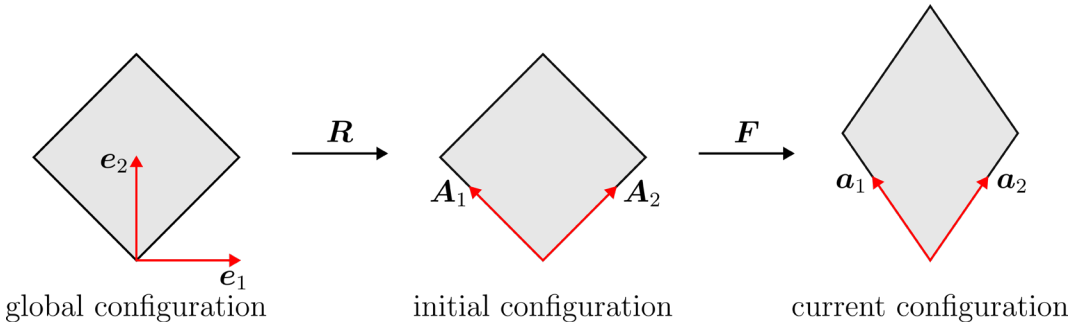

Fig. 2: Schematic illustration of the transformations between global, initial, and current configuration.

Numerical verification

To investigate the WLSQ gradient method for forming simulation of NCF a planar small-scale example is examined. The two applied element-based fields of a synthetic scalar variable are shown in Figure 3. For investigational purposes, in both depicted cases the initial and current configurations coincide. The applied field in Figure 3 a) will be referred to as diagonal distribution. The rotation matrix $\boldsymbol{R}_{\text{diag}}$ corresponds to a rotation of 45° about the $\boldsymbol{e}_3$-axis. The scalar field shown in Figure 3 b) will be referred to as horizontal distribution. All configurations coincide and it follows that $\boldsymbol{R}_{\text{horiz}} = \boldsymbol{I}$.

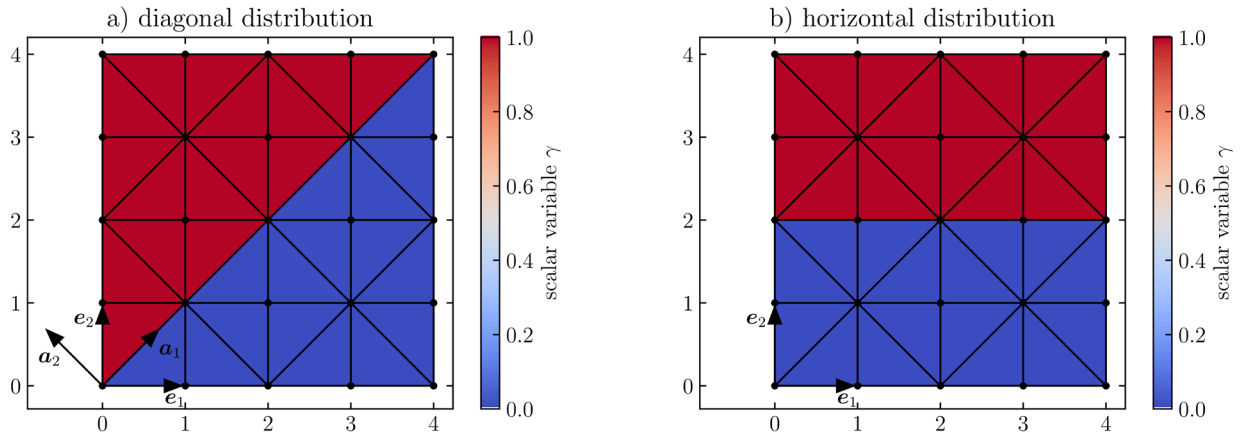

Fig. 3: Visualization of the two considered distributions of a synthetic element-based scalar variable γ.

The calculated gradient of the synthetic scalar variable is shown in Figure 4. The elements located at the outer edge of the meshes are not fully surrounded by neighbor elements. Whenever a reference element is missing one neighboring element and if the remaining neighboring element has a different value of the scalar field variable than the reference element ($\Delta\gamma_{IJ} \neq 0$), this leads to so-called boundary effects. These boundary effects are recognizable in the bottom left and top right corner in Figure 4. Due to the undeformed state of the mesh and the fact that triangle elements are used, the missing element leads to one of the two components being zero (cf. Fig. 4 a) and b)). This depends on whether the vector $\boldsymbol{d}_{\mathrm{norm},IJ}$ of the missing element J contains the $\boldsymbol{e}_1$- or the $\boldsymbol{e}_2$-direction. If $\boldsymbol{d}_{\mathrm{norm},IJ} = |\boldsymbol{e}_1|$ does not appear in the matrix $\boldsymbol{D}_{\mathrm{norm}}$ it results in the gradient component in $\boldsymbol{e}_2$-direction being zero. The non-zero components then have a value that exhibits the value of the scalar field variable γ. The gradient components of the inner elements in Figures 4 a) and b) in the global configuration are equal in amount. Rotating the gradient to the current configuration using $\boldsymbol{R}_{\mathrm{diag}}$ results in disappearing of the gradient component in the direction of $\boldsymbol{a}_1$ for the inner elements (cf. Figure 4 c)). Only the gradient in the $\boldsymbol{a}_2$-direction exists in case of neglecting the elements with a boundary influence. The gradient component's magnitude of the inner elements is less than that of the element-based scalar variable. However, the value of the gradient is also dependent on the choice of the weights. In this work a weight with $\mathrm{p} = 2$ is used. Comparing the gradient components with the given diagonal distribution, this is a sufficient result.

Applying the WLSQ gradient method on the horizontal distribution leads to the result depicted in Figure 5. The Figure shows that a gradient occurs in the $\boldsymbol{e}_1$-direction. Comparing this to the given horizontal distribution, the existence of the gradient component in the direction of $\boldsymbol{e}_1$ is not desirable. However, the occurrence of a gradient in the $\boldsymbol{e}_1$-direction cannot be prevented. The reason for this is the WLSQ method, as the direction between the reference and neighboring element $\boldsymbol{d}_{\mathrm{norm},IJ}$ in the matrix $\boldsymbol{D}_{\mathrm{norm}}$ also influences the gradient although the difference between the scalar variable $\Delta\gamma_{IJ}$ vanishes. However, this effect is a local error that disappears in a global consideration when integrating the incorrect component over the domain. It can be stated that the gradient in the $\boldsymbol{e}_2$-direction is 1.5 times greater in terms of the magnitude.

Materials Research Proceedings 41 (2024) 467-476 https://doi.org/10.21741/9781644903131-52

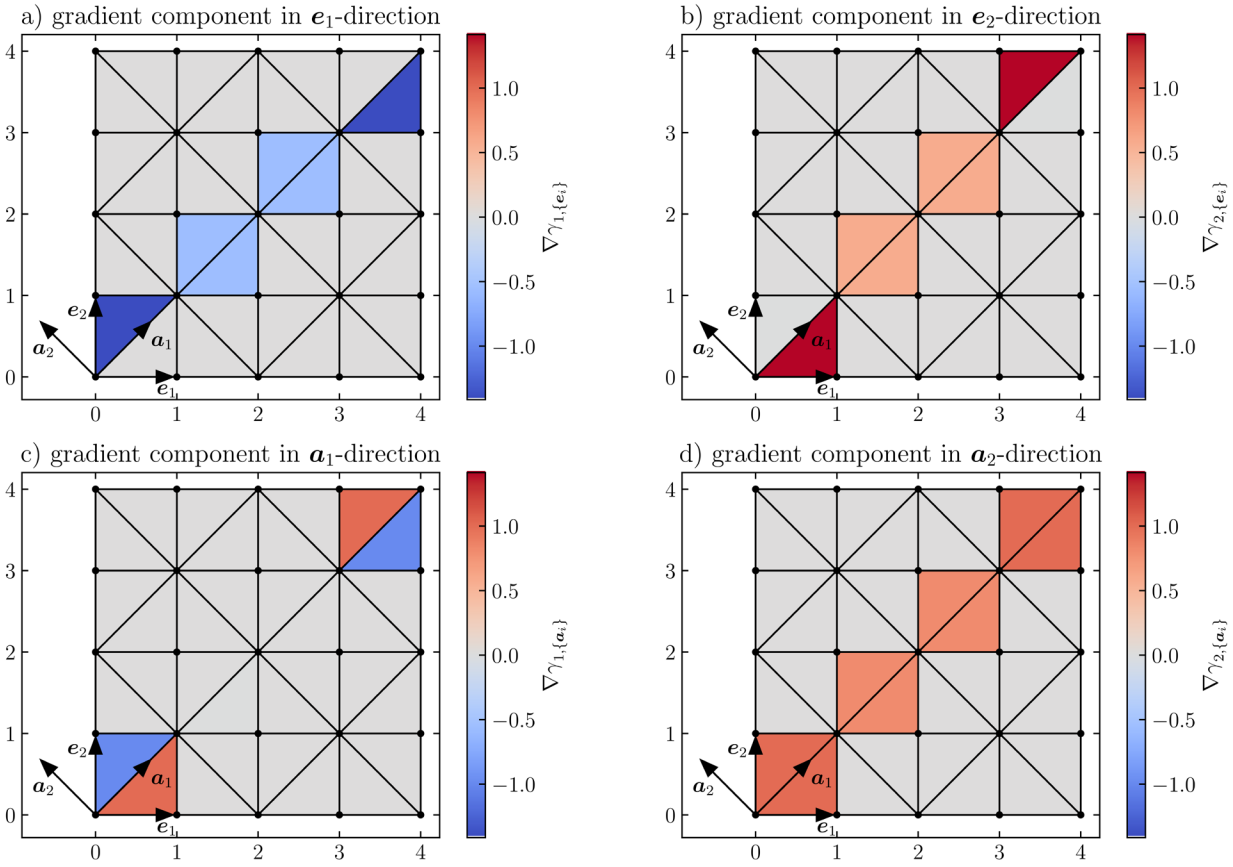

Fig. 4: Results of the gradient component 1 *a) and component* 2 *b) in the global configuration* $\{\boldsymbol{e}_i\}$ *and component* 1 *c) and component* 2 *d) in the current configuration* $\{\boldsymbol{a}_i\}$ *of the diagonal distribution.*

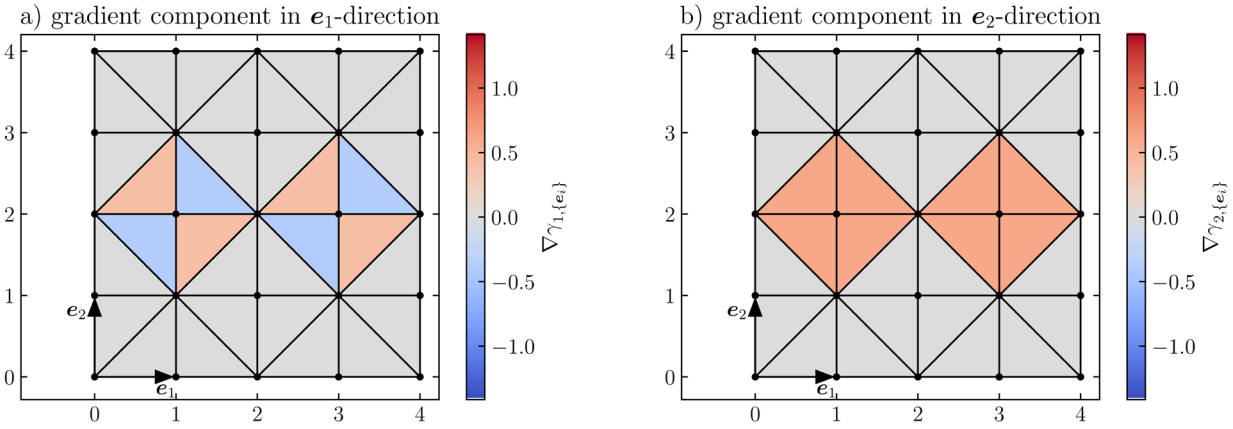

Fig. 5: Results of the gradient component 1 *a) and component* 2 *b) in the global configuration* $\{\boldsymbol{e}_i\}$ *of the horizontal distribution. The current configuration* $\{\boldsymbol{a}_i\}$ *equals the global configuration* $\{\boldsymbol{e}_i\}$ *in this case.*

As shown in the above small-scale examples, the WLSQ gradient method as presented here is not yet able to make a quantitative, but only a qualitative statement on the occurrence of a gradient of an element-based scalar variable. It is sufficient to localize the transition zones between areas with a high deviation in a scalar variable such as the shear angle. The potential of the method can be seen, but challenges still need to be overcome. In Figure 4 the problem of elements at the

boundary is pointed out, while an incorrect component is predicted at local scale, which disappears in a global consideration (cf. Fig. 5).

Application on the bias extension test

The model for simulating the BET is created in ABAQUS/EXPLICIT. The dimensions of the considered UD-NCF are 320 mm × 160 mm. The geometry is discretized using 4096 triangular elements, each with an edge length of 5 mm. The nodes at $x_2 = 0$ mm are pinned in their degrees of freedom. The simulation is carried out displacement-controlled, with the displacement of $u_2 = 80$ mm being applied to the nodes at $x_2 = 320$ mm. The fibers and stitching are initially orthogonal, which is reflected by the $\{\boldsymbol{A}_i\}$-frame. The fibers are oriented along the $\boldsymbol{A}_1$-direction and the stitching along the $\boldsymbol{A}_2$-direction. To transfer the $\{\boldsymbol{A}_i\}$-frame to the global frame $\{\boldsymbol{e}_i\}$ the rotation matrix $\boldsymbol{R}_{\text{diag}}$ is used.

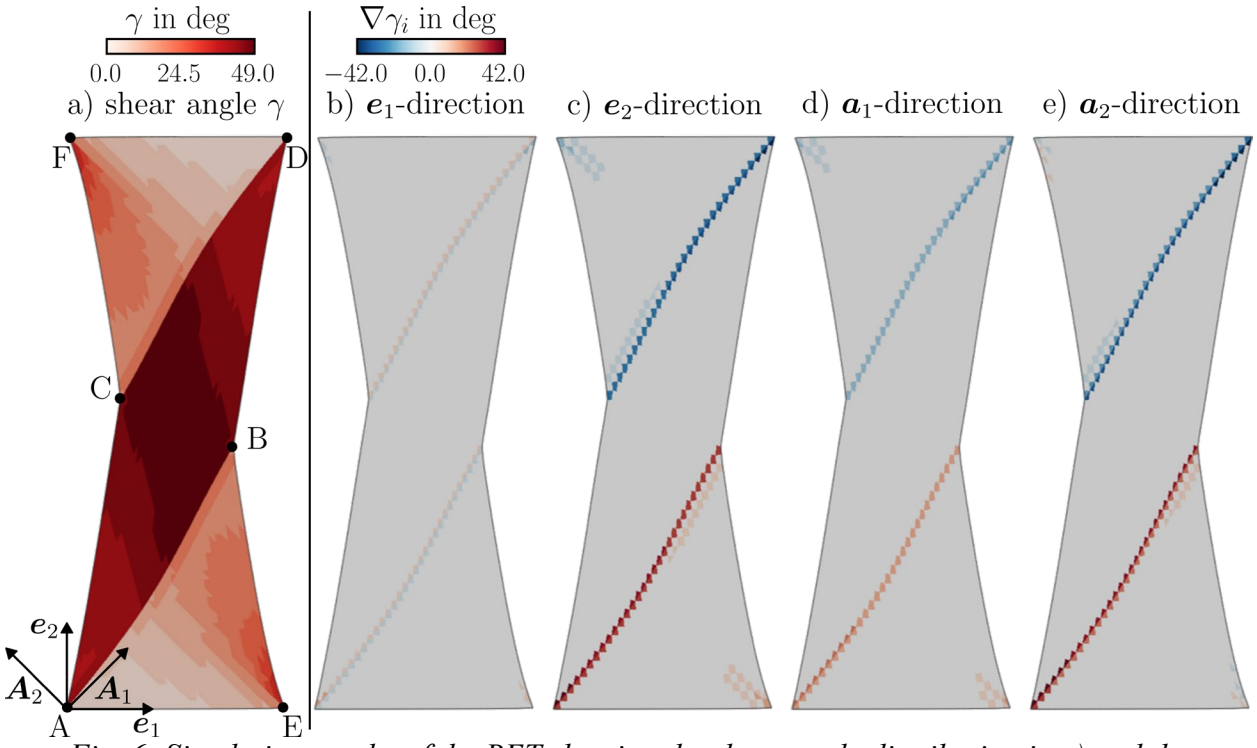

Fig. 6: Simulation results of the BET showing the shear angle distribution in a) and the components of the gradients in the global b), c) and current d), e) configuration.

The material model chosen is the hyperelastic St. Venant-Kirchhoff model [28]. The model is implemented in the user subroutine VUMAT The formulation for the second Piola–Kirchhoff stress tensor $\boldsymbol{S}$ reads

$$\boldsymbol{S} = \mathbb{C}[\boldsymbol{E}], \tag{7}$$

where $\mathbb{C}$ is the stiffness tensor and $\boldsymbol{E}$ is the Green-Lagrangian strain tensor. The stiffnesses remain constant during the simulation and their values are selected to qualitatively represent the forming behavior of the NCF for simulating the BET. Since the fibers are significantly stiffer than the stitching, an order of magnitude of three is defined between their stiffnesses. Consequently, for the Young's modulus of the fiber follows $E_1 = 1000$ MPa and for Young's modulus of the stitching $E_2 = 1$ MPa. For the shear stiffness a shear modulus $G_{12} = 0.5$ MPa is used. If the shear modulus is set too low, the middle section of the NCF will collapse. The Poisson's ratio is omitted. Since

the BET is a planar problem these material parameters are sufficient to describe and construct the orthotropic stiffness tensor $\mathbb{C}$ in Eq. (7).

In Figure 6 the simulation results of the BET are visualized. The outermost row of elements is neglected in the figure because the gradient has a significantly higher value there than in the interior of the mesh due to the boundary effects. Since the fiber and stitching stiffnesses are three orders of magnitude apart, the three zones with constant shear deformation, as characteristic for woven fabrics, do not occur [7]. The deformation in the middle zone is not a pure shear deformation for UD-NCF with a maximal shear angle $\gamma \approx 49\,°$ (cf. Figure 6 a)). This behavior was demonstrated experimentally on the BET [6,10]. Along the connection of $\overline{\mathrm{AB}}$ as well as $\overline{\mathrm{CD}}$ there is a steep decrease in the shear angle. In addition, a smaller deviation can be seen in the vicinity of E and F respectively. Applying the introduced WLSQ method leads to the gradient components shown in Figure 6 b)-e). The gradient components along the transition zones $\overline{\mathrm{AB}}$ and $\overline{\mathrm{CD}}$ stand out particularly. In the remaining mesh except the areas around E and F, the gradient components show very small values $\nabla\gamma_i < 1.0\,°$. The component in the $\boldsymbol{e}_2$-direction is more pronounced than in the $\boldsymbol{e}_1$-direction. The rotation and application of the deformation gradient leads to the components in the material configuration $\{\boldsymbol{a}_i\}$ in Figure 6 d) and e). Similarly, it is observable that the component along the orientation of the fibers $\boldsymbol{a}_1$ is smaller than in the direction of the stitching $\boldsymbol{a}_2$. The qualitative agreement with the shear angle distribution in Figure 6 a) is thus given.

Conclusion and outlook

A general framework in ABAQUS/EXPLICIT which allows to consider localized draping effects in macroscopic forming simulations is presented. For this purpose, a combination of external FORTRAN subroutines and user subroutines is used to implement a neighboring element method. The neighbor information stored in global arrays can be retrieved by any other subroutine at runtime. The functionality of the neighboring element method is demonstrated in the calculation of a cross element gradient of a scalar element-based variable utilizing the cell-average weighted least-squares (WLSQ) gradient method. The WLSQ gradient method is first examined on two small-scale examples. It is shown that a qualitative statement about the occurrence of gradients can be made. Applied on macroscopic simulation of the bias-extension test (BET), the transition zones occurring at deviating shear angles are detected.

To improve of the WLSQ gradient method further extensions are necessary. These include the consideration of additional stencils, the mitigation of the boundary effects, and addressing the local error of the gradient components. Subsequently the gradient of the shear angle computed using the WLSQ method is to be integrated into a hyperelastic material approach based on pseudo-invariants by using a suitable coupling mechanism in order to model the localized fiber roving slippage in the transition zones.

Acknowledgement

The authors would like to thank the German Federal Ministry for Economic Affairs and Climate Action (BMWK) for funding the LuFo research project Electra (20W1912D), for which the work has been carried out. Furthermore, the authors would like to thank the Deutsche Forschungsgemeinschaft (DFG, German Research Foundation) and the French National Research Agency (ANR) for funding the collaborative project “Composite forming simulation for non-crimp fabrics based on generalized continuum approaches” (DFG: 431354059, ANR: ANR-19-CE06-0031-012), in which essential preliminary work had been conducted. The work is also part of the Heisenberg project “Digitalization of fiber-reinforced polymer processes for resource-efficient manufacturing of lightweight components”, funded by the DFG (798455807141).

References

[1] F. Henning, L. Kärger, D. Dörr, F.J. Schirmaier, J. Seuffert, A. Bernath, Fast processing and continuous simulation of automotive structural composite components, Composites Science and Technology 171 (2019) 261–279. https://doi.org/10.1016/j.compscitech.2018.12.007

[2] C. Krogh, J.A. Kepler, J. Jakobsen, Pure and simple: investigating the in-plane shear kinematics of a quasi-unidirectional glass fiber non-crimp fabric using the bias-extension test, Int J Mater Form 19 (2021) 1483–1495. https://doi.org/10.1007/s12289-021-01642-8

[3] P. Böhler, F. Härtel, P. Middendorf, Identification of Forming Limits for Unidirectional Carbon Textiles in Reality and Mesoscopic Simulation, Key Engineering Materials 554-557 (2013) 423–432. https://doi.org/10.4028/www.scientific.net/KEM.554-557.423

[4] N. Hamila, P. Boisse, Locking in simulation of composite reinforcement deformations. Analysis and treatment, Composites Part A: Applied Science and Manufacturing 53 (2013) 109–117. https://doi.org/10.1016/j.compositesa.2013.06.001

[5] E. Kunze, S. Galkin, R. Böhm, M. Gude, L. Kärger, The Impact of Draping Effects on the Stiffness and Failure Behavior of Unidirectional Non-Crimp Fabric Fiber Reinforced Composites, Materials 13 (2020). https://doi.org/10.3390/ma13132959

[6] F.J. Schirmaier, K.A. Weidenmann, L. Kärger, F. Henning, Characterisation of the draping behaviour of unidirectional non-crimp fabrics (UD-NCF), Composites Part A: Applied Science and Manufacturing 80 (2016) 28–38. https://doi.org/10.1016/j.compositesa.2015.10.004

[7] G. Lebrun, M.N. Bureau, J. Denault, Evaluation of bias-extension and picture-frame test methods for the measurement of intraply shear properties of PP/glass commingled fabrics, Selected Papers from the Symposium on Design and Manufacturing of Composites 61 (2003) 341–352. https://doi.org/10.1016/S0263-8223(03)00057-6

[8] J. Launay, G. Hivet, A.V. Duong, P. Boisse, Experimental analysis of the influence of tensions on in plane shear behaviour of woven composite reinforcements, Composites Science and Technology 68 (2008) 506–515. https://doi.org/10.1016/j.compscitech.2007.06.021

[9] S. Bel, P. Boisse, F. Dumont, Analyses of the Deformation Mechanisms of Non-Crimp Fabric Composite Reinforcements during Preforming, Applied Composite Materials 19 (2012) 513–528. https://doi.org/10.1007/s10443-011-9207-x

[10] B. Schäfer, R. Zheng, N. Naouar, L. Kärger, Membrane behavior of uni- and bidirectional non-crimp fabrics in off-axis-tension tests, Int J Mater Form 16 (2023) 1–15. https://doi.org/10.1007/s12289-023-01792-x

[11] M.A. Khan, T. Mabrouki, E. Vidal-Sallé, P. Boisse, Numerical and experimental analyses of woven composite reinforcement forming using a hypoelastic behaviour. Application to the double dome benchmark, Journal of Materials Processing Technology 210 (2010) 378–388. https://doi.org/10.1016/j.jmatprotec.2009.09.027

[12] M. Machado, M. Fischlschweiger, Z. Major, A rate-dependent non-orthogonal constitutive model for describing shear behaviour of woven reinforced thermoplastic composites, Composites Part A: Applied Science and Manufacturing 80 (2016) 194–203. https://doi.org/10.1016/j.compositesa.2015.10.028

[13] F. Schäfer, H.O. Werner, F. Henning, L. Kärger, A hyperelastic material model considering biaxial coupling of tension–compression and shear for the forming simulation of woven fabrics, Composites Part A: Applied Science and Manufacturing 165 (2023). https://doi.org/10.1016/j.compositesa.2022.107323

[14] Y. Gong, D. Yan, Y. Yao, R. Wei, H. Hu, P. Xu, X. Peng, An Anisotropic Hyperelastic Constitutive Model with Tension–Shear Coupling for Woven Composite Reinforcements, Int. J. Appl. Mechanics 09 (2017). https://doi.org/10.1142/S1758825117500831

[15] Y. Yao, X. Huang, X. Peng, P. Liu, G. Youkun, An anisotropic hyperelastic constitutive model for plain weave fabric considering biaxial tension coupling, Textile Research Journal 89 (2019) 434–444. https://doi.org/10.1177/0040517517748495

[16] S. Lomov, D. Ivanov, I. Verpoest, M. Zako, T. Kurashiki, H. Nakai, S. Hirosawa, Meso-FE modelling of textile composites: Road map, data flow and algorithms, Composites Science and Technology 67 (2007) 1870–1891. https://doi.org/10.1016/j.compscitech.2006.10.017

[17] J. Sirtautas, A.K. Pickett, P. Lépicier, A mesoscopic model for coupled drape-infusion simulation of biaxial Non-Crimp Fabric, Composites Part B: Engineering 47 (2013) 48–57. https://doi.org/10.1016/j.compositesb.2012.09.088

[18] G. Creech, A. Pickett, Meso-modelling of Non-Crimp Fabric composites for coupled drape and failure analysis, Journal of Materials Science 41 (2006) 6725–6736. https://doi.org/10.1007/s10853-006-0213-6

[19] F.J. Schirmaier, D. Dörr, F. Henning, L. Kärger, A macroscopic approach to simulate the forming behaviour of stitched unidirectional non-crimp fabrics (UD-NCF), Composites Part A: Applied Science and Manufacturing 102 (2017) 322–335. https://doi.org/10.1016/j.compositesa.2017.08.009

[20] B. Schäfer, S. Haas, P. Boisse, L. Kärger, Investigation of the Membrane Behavior of UD-NCF in Macroscopic Forming Simulations, Key Engineering Materials 926 (2022) 1413–1422. https://doi.org/10.4028/p-2977b4

[21] V.N. Khiêm, H. Krieger, M. Itskov, T. Gries, S.E. Stapleton, An averaging based hyperelastic modeling and experimental analysis of non-crimp fabrics, International Journal of Solids and Structures. https://doi.org/10.1016/j.ijsolstr.2016.12.018

[22] B. Schäfer, D. Dörr, R. Zheng, N. Naouar, L. Kärge, A hyperelastic approach for modeling the membrane behavior in finite element forming simulation of unidirectional non-crimp fabrics (UD-NCF), Composites Part A: Applied Science and Manufacturing (2023).

[23] Q. Steer, J. Colmars, N. Naouar, P. Boisse, Modeling and analysis of in-plane bending in fibrous reinforcements with rotation-free shell finite elements., International Journal of Solids and Structures 222-223 (2021). https://doi.org/10.1016/j.ijsolstr.2021.03.001

[24] Y. Aimène, E. Vidal-Sallé, B. Hagège, F. Sidoroff, P. Boisse, A Hyperelastic Approach for Composite Reinforcement Large Deformation Analysis, Journal of Composite Materials 44 (2010) 5–26. https://doi.org/10.1177/0021998309345348

[25] C.T. Poppe, C. Krauß, F. Albrecht, L. Kärger, A 3D process simulation model for wet compression moulding, Composites Part A: Applied Science and Manufacturing 50 (2021) 106379. https://doi.org/10.1016/j.compositesa.2021.106379

[26] J.A. White, H. Nishikawa, R.A. Baurle, Weighted Least-squares Cell-Average Gradient Construction Methods For The VULCAN-CFD Second-Order Accurate Unstructured Grid Cell-Centered Finite-Volume Solver, AIAA Scitech 2019 Forum. https://doi.org/10.2514/6.2019-0127

[27] S. Seo, C. Lee, E. Kim, K. Yune, C. Kim, Least-square Switching Process for Accurate and Efficient Gradient Estimation on Unstructured Grid, Journal of the Korean Society for Industrial and Applied Mathematics 24 (2020) 1–22. https://doi.org/10.12941/JKSIAM.2020.24.001

[28] T. Belytschko, W.K. Liu, B. Moran, K.I. Elkhodary, Nonlinear finite elements for continua and structures, 2nd ed., Wiley, Chichester, 2014.